



---

*Review*

## **Silicon nanocrystals embedded in oxide films grown by magnetron sputtering**

**Larysa Khomenkova<sup>1,\*</sup>, Mykola Baran<sup>1</sup>, Jędrzej Jędrzejewski<sup>2</sup>, Caroline Bonafos<sup>3</sup>, Vincent Paillard<sup>3</sup>, Yevgen Venger<sup>1</sup>, Isaac Balberg<sup>2</sup>, and Nadiia Korsunskaa<sup>1</sup>**

<sup>1</sup> V. Lashkaryov ISP of NASU, 45 Pr. Nauky, 03028 Kyiv, Ukraine

<sup>2</sup> Racah Institute of Physics, Hebrew University, 91904 Jerusalem, Israel

<sup>3</sup> CEMES/CNRS, University of Toulouse, 29 rue J. Marvig 31055 Toulouse Cedex 4, France

\* **Correspondence:** E-mail: khomen@ukr.net; Tel: +38-044-525-7557;  
Fax: +38-044-525-8342.

**Abstract:** This paper presents a comparison of the results that we obtained and reported over the last few years on the structural, optical and light emitting properties of Si-SiO<sub>2</sub> and Si-Al<sub>2</sub>O<sub>3</sub> films that were fabricated using a specific configuration of RF magnetron sputtering. In these films the Si volume fraction,  $x$ , varies along the film (which is typically 14 cm long) from a value of  $\sim 0.1$  at one end to  $\sim 0.9$  at the other end. For the films with  $x > 0.3$ , the formation of amorphous Si clusters was observed in as-deposited Si-SiO<sub>2</sub> and Si-Al<sub>2</sub>O<sub>3</sub> films. Si nanocrystals (Si-ncs) were generated by high-temperature annealing of the films in nitrogen atmosphere. We found that two processes can contribute to the Si-ncs formation: (i) the crystallization of the existing amorphous Si inclusions in the as-deposited films, and (ii) the thermally stimulated phase separation. Process (i) can be responsible for the independence of Si-ncs mean sizes on  $x$  in annealed films with  $x > 0.5$ . At the same time, difference in the structural and the light emitting properties of the two types of films was observed. For the samples of the same  $x$ , the Si-ncs embedded in the Al<sub>2</sub>O<sub>3</sub> host were found to be larger than the Si-ncs in the SiO<sub>2</sub> host. This phenomenon can be explained by the lower temperature required for phase separation in Si-Al<sub>2</sub>O<sub>3</sub> or by the lower temperature of the crystallization of Si-ncs in alumina. The latter suggestion is supported by Raman scattering and electron paramagnetic resonance spectra. In contrast with the Si-SiO<sub>2</sub>, the Si-ncs embedded in Si-Al<sub>2</sub>O<sub>3</sub> films were found to be under tensile stress. This effect was explained by the strains at the interfaces between the film and silica substrate as well as between the Si inclusions and the Al<sub>2</sub>O<sub>3</sub> host. It was also shown that exciton recombination in Si-ncs is the dominant radiative channel in Si-SiO<sub>2</sub> films, while the emission from the oxide defects dominates in Si-Al<sub>2</sub>O<sub>3</sub> films. This can be due to the high number of non-radiative defects at

Si-ncs/ $\text{Al}_2\text{O}_3$  interface, which is confirmed by our electron paramagnetic resonance data and is consistent with our above suggestion of mechanical stresses in the Si- $\text{Al}_2\text{O}_3$  films.

**Keywords:** Si nanocrystals;  $\text{SiO}_2$ ;  $\text{Al}_2\text{O}_3$ ; luminescence; defects

## 1. Introduction

One of the important tasks of photonics and microelectronics is realization of low-cost integrated optoelectronic devices based on silicon-compatible CMOS technology (i.e. all-in-one Si chip). In this regard, silicon nanocrystallites (Si-ncs) attract considerable interest due to significant transformation of their optical and electrical properties caused by quantum-confinement effect [1,2,3].

Light-emitting Si-ncs embedded in dielectric hosts offer potential applications in optoelectronic devices because of their compatibility with the existing manufacturing infrastructure for silicon integrated circuits. Among different dielectric materials, silicon oxide is the most addressed as a host for Si-ncs [4–11]. The properties of Si-ncs embedded in  $\text{SiO}_2$  systems have been deeply investigated during last decades [3–11]. It is widely accepted by now that bright luminescence at room temperature is caused by the recombination of excitons in the Si-ncs. The monitoring of their size distribution allowed fine wavelength tuning of this emission in wide spectral range. On the other hand, it was also demonstrated that silicon oxide defects can be the source of observable light emitting process.

In view of the interest in the Si-ncs systems, the mechanism of the Si-ncs formation in  $\text{SiO}_2$  was widely investigated. It was shown that the fabrication conditions and post-processing affect the sizes and spatial distribution of Si-ncs in oxide host. Based on the obtained results and good compatibility with existing CMOS technology an application of Si-nc- $\text{SiO}_2$  nanomaterials for microelectronics and photonics was suggested [12,13]. However, the downscaling of microelectronic devices requires the elaboration of novel materials to overcome bottleneck of silicon oxide as gate material. In this regard, other dielectrics such as  $\text{HfO}_2$  and  $\text{Al}_2\text{O}_3$  are considered as promising gate dielectrics. It was also demonstrated that Si-ncs embedded in such high-k matrix can improve non-volatile memory devices [14,15,16]. However, these alternative dielectrics were not well addressed in terms of optical application. At the same time, they have a higher refractive index (for instance,  $n_{\text{Al}_2\text{O}_3} = 1.73$  vs.  $n_{\text{SiO}_2} = 1.46$  at 1.95 eV) that offers better light confinement. Along with good solubility of rare-earth ions in such materials, their photonic application becomes conceivable. Alumina-based waveguides have been developed by sol-gel techniques for optical communications [17,18]. Only few groups reported on Si-ncs- $\text{Al}_2\text{O}_3$  materials fabricated by ion implantation or electron beam evaporation [19,20,21]. At the same time, magnetron sputtering was rarely considered for fabrication of  $\text{Al}_2\text{O}_3$  materials with embedded Si-ncs [22–26] in spite of the relative simplicity of the co-sputtering technique and its compatibility with CMOS technology [7,9,10,11].

The purpose of this paper is to describe the fabrication and properties of the Si-ncs- $\text{Al}_2\text{O}_3$  and Si-ncs- $\text{SiO}_2$  systems as they emerge from our studies in the last years. It appears to us that the integration of the various results that we obtained and reported previously [5,6,7,9,23–26], with the additional new results obtained by transmission electron microscopy method that we first report here, enables us now to provide a comprehensive state-of-the-art comparison between the structure and the physical properties of these systems.

Basically, the present paper demonstrates the application of magnetron sputtering for the fabrication of Si-rich- $\text{Al}_2\text{O}_3$  and Si-rich- $\text{SiO}_2$  films with different Si contents. We compare here the results obtained for the Si-ncs embedded in  $\text{Al}_2\text{O}_3$  and  $\text{SiO}_2$  hosts. In particular, the study of the effect of post-deposition processing on the evolution of the microstructure of the corresponding films and their optic and luminescent properties enable us to get information about the Si-ncs formation and the nature of the emitting centers in such films with different Si content. In turn, our conclusions are expected to improve the understanding needed for getting a better control of the luminescent properties of these materials.

## 2. Materials and Method

### 2.1. Sample preparation

The Si- $\text{Al}_2\text{O}_3$  and Si- $\text{SiO}_2$  films were deposited by radio frequency bottom-up magnetron co-sputtering from two spaced-apart targets (of high quality Si and nearly stoichiometric oxide ( $\text{Al}_2\text{O}_3$  or  $\text{SiO}_2$ )) in pure argon plasma at room temperature. The background vacuum in the sputtering chamber was about  $1 \times 10^{-5}$  Pa prior to the deposition. The RF power densities applied to Si,  $\text{SiO}_2$  and  $\text{Al}_2\text{O}_3$  targets were  $0.48 \text{ W/cm}^2$ ,  $0.74 \text{ W/cm}^2$  and  $0.98 \text{ W/cm}^2$ , respectively. The deposition time was 250 min for Si- $\text{Al}_2\text{O}_3$  and 180 min for Si- $\text{SiO}_2$  films.

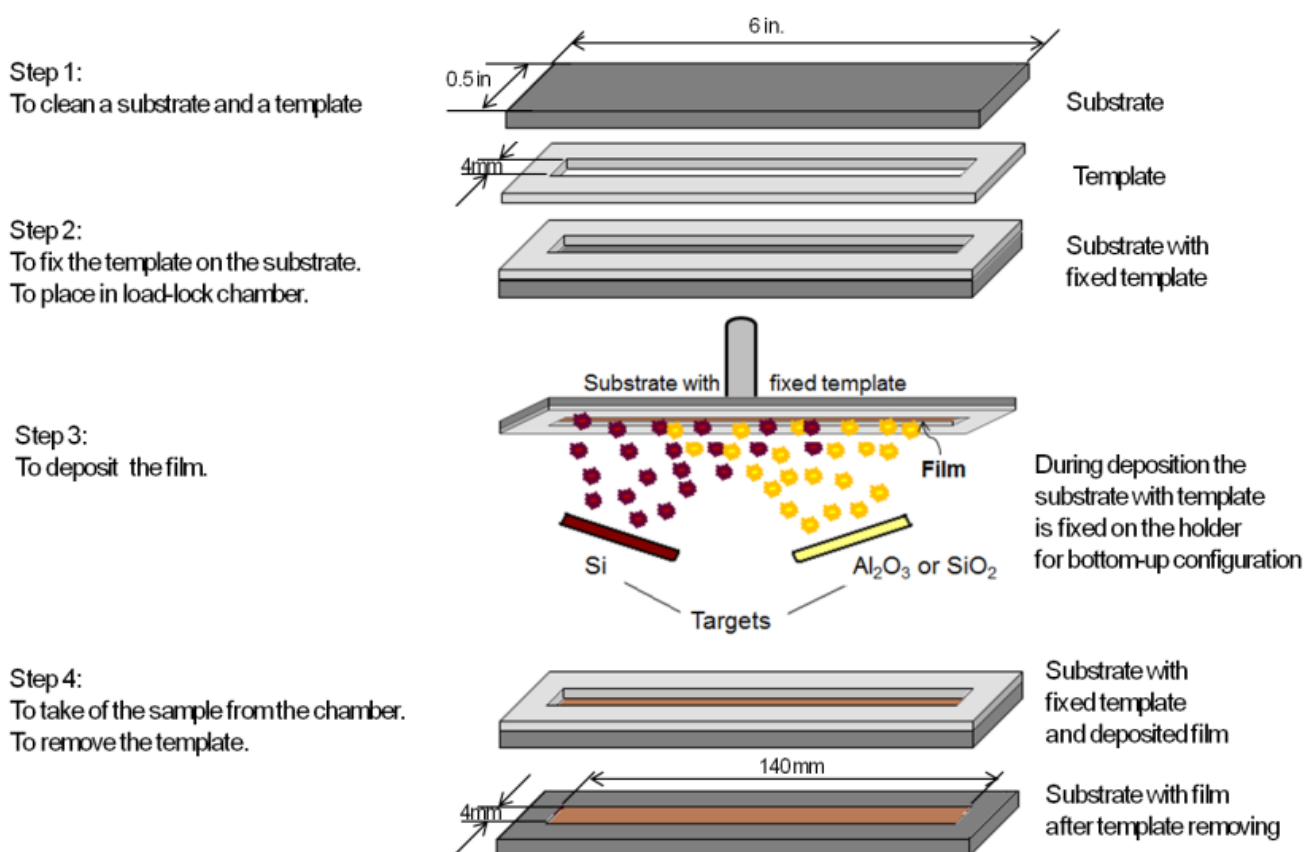


**Figure 1.** A schematic illustration of the co-sputtering deposition procedure.

The deposition was performed on long non-rotated fused silica substrates (Fig.1). The substrate was 6 inches long and 0.5 inches wide. The deposited layers were about 140 mm long and about 4 mm wide as formed by a proper template (see Fig. 1). Prior to deposition, the substrate and template were submitted to standard RCA cleaning procedure and then placed in a load-lock chamber. Such approach allowed to prepare the films with gradual variation of the Si volume fraction ( $x$ ) along the film length within one deposition run at fixed powers applied to the cathodes (Fig.2) [6,23,24].

As-deposited long films were annealed either in a conventional horizontal furnace at 1150 °C for 30 min under a nitrogen flow (CA treatment) or in a rapid thermal processing tool at 1050 °C for 1 min in air (RTA treatment). The annealing of such long films enables to stimulate simultaneously the phase separation and Si-ncs formation in the films with different Si excess content. Annealed long substrate with the film on it was cut to smaller (1 cm in the length) segments (hereafter the samples) and their properties were investigated as a function of the Si excess.

## 2.2. Experimental methods

To investigate the microstructure and luminescent properties of the films, a Horiba Jobin-Yvon T-64000 Raman spectrometer equipped with confocal microscope and automated piezo-driven XYZ stage was used. The micro-Raman scattering and micro-photoluminescence spectra were recorded in the 100–900-cm<sup>-1</sup> and in 500–900-nm spectral ranges, respectively. A 488.0-nm line of Ar-Kr ion laser was used for excitation. The laser power on the sample surface was always kept below 5 mW (at 150- $\mu$ m beam diameter) to obtain the best signal-to-noise ratio, preventing a laser heating of the investigated sample. The spectral resolution of the spectrometer was less than 0.15 cm<sup>-1</sup>. In addition, standard photoluminescence (PL) spectra were excited by the 488-nm line of an Ar<sup>+</sup> laser or the 337-nm line of N<sub>2</sub> laser. The PL was recorded by a photomultiplier or a cooled Ge detector. The micro- and standard PL as well as micro-Raman scattering spectra were measured at three points of each sample (i.e. in the center and at 1.5-mm from sample edges). The measurements reported here were performed at 300 K and at 80 K.

Our X-ray diffraction (XRD) study was carried out using Philips X'Pert-MRD diffractometer with Cu K $\alpha$ -radiation ( $\lambda = 0.15418$  nm) in a grazing geometry to increase the beam-film interaction volume. To obtain information on the defect structure of the samples, the electron paramagnetic resonance (EPR) spectra were measured using a Varian-12 spectrometer. The accuracy of the determination of g-factor values was  $\Delta g = \pm 0.0005$ .

To study the chemical composition of the films, their refractive index and thickness, spectroscopic ellipsometry measurement was performed by means of a Jobin-Yvon ellipsometer (UVISEL, HORIBA Ltd., Kyoto, Japan), where the incident light was scanned in the range of 1.5 to 4.5 eV under an incident angle of 66.3°. The beam spot was 1 mm in diameter. The spectra were recorded at the central point of each sample. To fit the experimental data we have used the DeltaPsi2 software (HORIBA Ltd., Kyoto, Japan) [27]. This allowed us to get information on the variation of the refractive index and thickness along the film length. The standard film thickness was determined by means of a Dektak 3030 Profilometer (Veeco, Plainview, NY, USA). The chemical composition of the layers was also controlled by the Auger spectroscopy. For these experiments, the layers were grown on silicon substrates. These spectra were measured by means of a RIBER LAS 2000 spectrometer and recorded in the range of 0–1000 eV with a resolution of 3.4 eV. The primary electron beam energy was 3 keV, and the area investigated was 100  $\times$  100  $\mu$ m<sup>2</sup> in the central part of each sample. The variation of the intensities of the Si LVV peak for «pure» silicon (at 92 eV), Si

LVV peak for Si in SiO<sub>2</sub> (at 76 eV) and the O KLL peak for oxygen (at 510 eV) was used to evaluate the relative compositions.

For getting more comprehensive information on the structural properties of the films, we have also applied, in the present work, a high-resolution TEM measurement. Cross-sectional specimens were prepared by the standard procedure involving grinding, dimpling and Ar<sup>+</sup> ion beam thinning until electron transparency. The samples were examined then by a FEI Tecnai microscope operating at 200 keV equipped with a field emission gun and a spherical aberration corrector.

### 3. Results

#### 3.1. Films composition and structural properties

The sputtering of the films on non-rotated long substrate used in the present study results in a continuous variation of the Si volume fraction ( $x$ ) along the film length. To estimate  $x$ , we followed the well-known procedure suggested by Hanak [28] and Abeles et al. [29]. They have shown that the composition of the film grown by co-sputtering of different targets can be predicted based on the volume contribution of each component. For our Si-SiO<sub>2</sub> and Si-Al<sub>2</sub>O<sub>3</sub> films this means that their composition is determined by volume contribution of each phase, Si and SiO<sub>2</sub> [5,6,7,9,10,11] or Si and Al<sub>2</sub>O<sub>3</sub> [23,24].

Our single-phase films of Si, SiO<sub>2</sub> or Al<sub>2</sub>O<sub>3</sub> were sputtered from the corresponding target using the same template. In our case, because of the fixed films width, the ratio of the thicknesses of the Si-only film and the corresponding composite film was used as the ratio of the film volumes [28,29].

For each single phase film, the variation of its thickness along the film length (i.e.  $d_{\text{Si}}$ ,  $d_{\text{SiO}_2}$  or  $d_{\text{Al}_2\text{O}_3}$ ) was measured directly (Fig.2a,b). For composite Si-SiO<sub>2</sub> and Si-Al<sub>2</sub>O<sub>3</sub> films, they were found to be  $d_{\text{Si-SiO}_2} = 800\text{--}1200$  nm (Fig.2a) and  $d_{\text{Si-Al}_2\text{O}_3} = 800\text{--}1500$  nm (Fig.2b), respectively. We have confirmed that the composite film's thickness is the additive function of the thicknesses of the Si and the corresponding oxide over the entire film length (Fig.2a,b).

This is true for the deposition of the films in pure Ar plasma that was previously confirmed for other composite films in Ref. [30]. Taking into account the variation of the thicknesses of the Si ( $d_{\text{Si}}$ ), the SiO<sub>2</sub> ( $d_{\text{Si-SiO}_2}$ ) or the Al<sub>2</sub>O<sub>3</sub> ( $d_{\text{Si-Al}_2\text{O}_3}$ ) layers (Fig.2a,b), the value of the Si volume fraction  $x$  in Si-SiO<sub>2</sub> and Si-Al<sub>2</sub>O<sub>3</sub> films was determined as  $x_{\text{Si-SiO}_2} = d_{\text{Si}}/d_{\text{Si-SiO}_2}$  or  $x_{\text{Si-Al}_2\text{O}_3} = d_{\text{Si}}/d_{\text{Si-Al}_2\text{O}_3}$  in corresponding points. The results are presented in Fig.2a,b. It is seen that the  $x$  changes in the range of  $x_{\text{Si-SiO}_2} = 0.18\text{--}0.7$  for Si-SiO<sub>2</sub> and  $x_{\text{Si-Al}_2\text{O}_3} = 0.15\text{--}0.95$  for Si-Al<sub>2</sub>O<sub>3</sub>.

The results shown in Fig. 2(a) were further confirmed by Auger spectroscopy for Si-rich SiO<sub>2</sub> layer (grown on Si substrate). It should be noted that the layers grown on silicon and fused silica substrates in the same deposition run have similar distribution of chemical composition along the layer [31]. The  $x_{\text{Si-SiO}_2}$  here was obtained as a ratio of the intensity of Si LVV peak at 98 eV (corresponding to single phase Si) to the total amount of Si in the co-sputtered film considered as sum of the intensities of Si LVV peaks of single phase Si and Si in SiO<sub>2</sub> [6]. A good agreement of the Auger data and those estimated from the thicknesses was obtained for  $x_{\text{Si-SiO}_2} > 0.5$  (Fig.2,a, star symbols), that demonstrates the accuracy of the above described method. However, Auger method is difficult to apply to the films with low Si content due to charging effect.

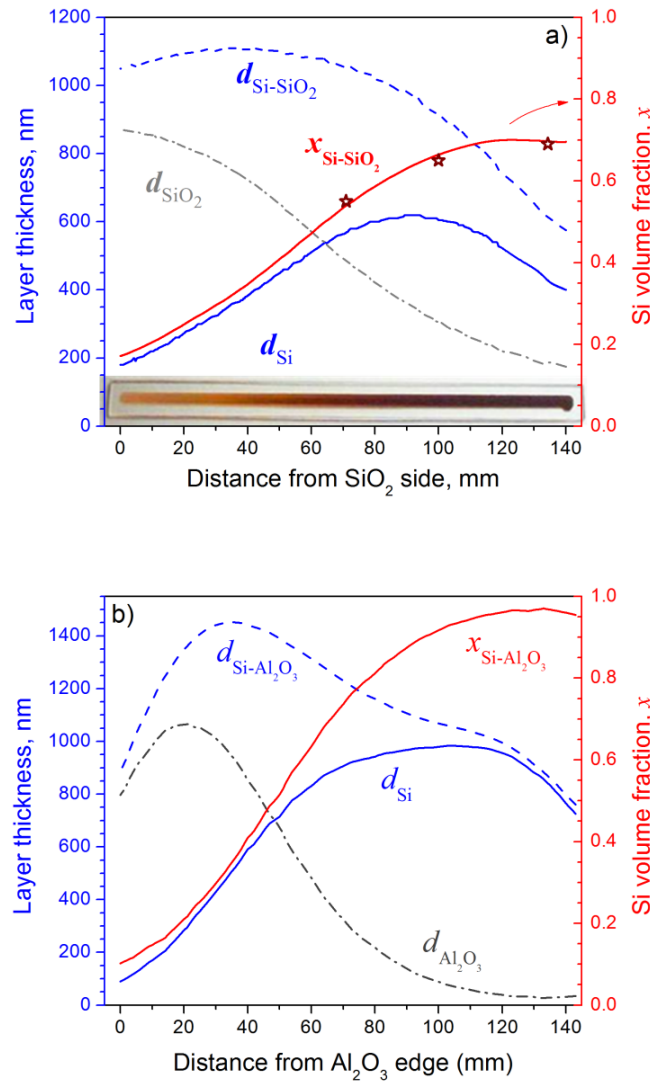


**Figure 2.** a) Variation of the thicknesses of single phase films (Si ( $d_{\text{Si}}$ ) and SiO<sub>2</sub> ( $d_{\text{SiO}_2}$ )) and composite Si-SiO<sub>2</sub> film ( $d_{\text{Si-SiO}_2}$ ), as well as the Si volume fraction ( $x_{\text{Si-SiO}_2}$ ) along the sample length; the stars (★) present the Si volume fraction in the Si-SiO<sub>2</sub> film estimated by Auger spectroscopy (taken from Ref. [29]); the inset shows the picture of a Si-SiO<sub>2</sub> film grown on fused silica substrate; b) variation of the thicknesses of the single phase films (Si ( $d_{\text{Si}}$ ) and Al<sub>2</sub>O<sub>3</sub> ( $d_{\text{Al}_2\text{O}_3}$ )) and composite Si-Al<sub>2</sub>O<sub>3</sub> film ( $d_{\text{Si-Al}_2\text{O}_3}$ ), as well as the Si volume fraction  $x_{\text{Si-Al}_2\text{O}_3}$ .

Another additional method that we used for the evaluation of  $x_{\text{Si-SiO}_2}$  and  $x_{\text{Si-Al}_2\text{O}_3}$  was spectroscopic ellipsometry. It is a fast, sensitive and non-destructive method for thin film characterization [14,32,33] that is widely used in semiconductor processing. The spectral dependencies of ellipsometric angles ( $\Psi$  and  $\Delta$ ) are defined from the fundamental equation of ellipsometry  $\overline{r_p} / \overline{r_s} = \tan \Psi \exp i\Delta$ , where  $\overline{r_p}$  and  $\overline{r_s}$  are the complex reflection coefficients for parallel and perpendicular light polarizations respectively. These dependencies of  $\Psi$  and  $\Delta$  can be fitted with appropriate modelling approaches to

extract the film thickness and optical constants (refractive index,  $n$ , and extinction coefficient,  $k$ ) based on the best fit between experimental and simulated spectra [14,32].

The dispersion relations, for as-deposited single phase films, sputtered from a single target (Si, SiO<sub>2</sub> or Al<sub>2</sub>O<sub>3</sub>) and for co-sputtered (Si-SiO<sub>2</sub> or Si-Al<sub>2</sub>O<sub>3</sub>) films, were obtained after fitting of ellipsometry data as follows. The dispersion relation for data fitting was based on the Forouhi-Bloomer model (FBM) that is well known for amorphous semiconductor and insulating films [34], using an improved parameterization [35]. More details of our application of this method were described previously [14,23]. The  $n$  values obtained for the single phase films are in agreement with the data of Refs. [36,37] and support the composition profiles obtained above by the two methods used.

Figure 3 represents the experimental  $n$  values at 1.9 eV light energy for Si-SiO<sub>2</sub> (Fig.3a) and Si-Al<sub>2</sub>O<sub>3</sub> (Fig.3b) films. The inset of Fig.3b shows the dispersion relation for Si-Al<sub>2</sub>O<sub>3</sub> samples with  $x_{\text{Si-Al}_2\text{O}_3} = 0.7$  (1), 0.4 (2) and 0.15 (3). It is seen that the dispersion curves for these films lie between the curves corresponded to pure Al<sub>2</sub>O<sub>3</sub> and amorphous silicon. They demonstrate gradual shift towards pure amorphous Si with Si content (Fig.3b, inset). For Si-Al<sub>2</sub>O<sub>3</sub> films this means that the film can be considered as a mixture of Al<sub>2</sub>O<sub>3</sub> and Si (or SiO<sub>*x*</sub> with  $x \ll 1$ ) rather than a mixture of Al<sub>2</sub>O<sub>3</sub> and SiO<sub>2</sub> similar to the case of Si-HfO<sub>2</sub> films [14].

All films were found to be amorphous as confirmed by Raman scattering and XRD data (see below) and thus, hereafter we consider our Si-rich-Al<sub>2</sub>O<sub>3</sub> film as an effective medium in which macroscopic properties are determined by the relative volume fractions of Si and Al<sub>2</sub>O<sub>3</sub>.

The relative fraction of Si phase in the Si-SiO<sub>2</sub> and Si-Al<sub>2</sub>O<sub>3</sub> films was determined using the Bruggeman effective medium approximation [38] as well as by the method described in [39]. The variation of dielectric function (i.e., refractive index) is defined then by the following two equations:

$$\sum_i x_i \frac{\varepsilon_i - \varepsilon}{\varepsilon_i + 2\varepsilon} = 0 \quad \text{and} \quad \sum_i x_i = 1$$

where  $\varepsilon_i$  and  $x_i$  are the complex optical dielectric function and volume fraction for the  $i$ -th component, respectively. We found that  $x$  varies from  $x \approx 0.92$  ( $n = 3.22 \pm 0.01$ ; Si-rich end) to  $x \approx 0.05$  ( $n = 1.73 \pm 0.01$ ; Si-poor end) for Si-Al<sub>2</sub>O<sub>3</sub> films [23]. Moreover, as shown in Fig.3b, the  $x_{\text{Si-Al}_2\text{O}_3}$  values estimated from both the thickness ratio (Fig.2b) and the refractive index here are in good agreement (within the experiment accuracy) in the  $0.15 < x < 0.7$  range. However, for Si-rich ( $x > 0.7$ ) and Si-poor ( $x < 0.1$ ) samples a lower refractive index was found, possibly caused by the presence of some other phases such as pores or SiO<sub>2</sub> with lower refractive index.

For Si-SiO<sub>2</sub> samples, the  $x_{\text{Si-SiO}_2}$  was also extracted from ellipsometry data and found to be  $x_{\text{Si-SiO}_2} = 0.2\text{--}0.7$  (Fig.3a) (as shown elsewhere [39]). The agreement between the  $x_{\text{Si-SiO}_2}$  values estimated with different methods is observed (Fig.3a). This demonstrates the utility of spectroscopic ellipsometry method for the estimation of film composition.

It is worth to note that the Si-Al<sub>2</sub>O<sub>3</sub> samples with  $x_{\text{Si-Al}_2\text{O}_3} > 0.7$  were found to be highly absorbed and they can be considered rather as Al<sub>2</sub>O<sub>3</sub>-rich-Si films than Si-rich alumina. Therefore, the sample analysis was restricted here to  $x_{\text{Si-Al}_2\text{O}_3} < 0.7$ .

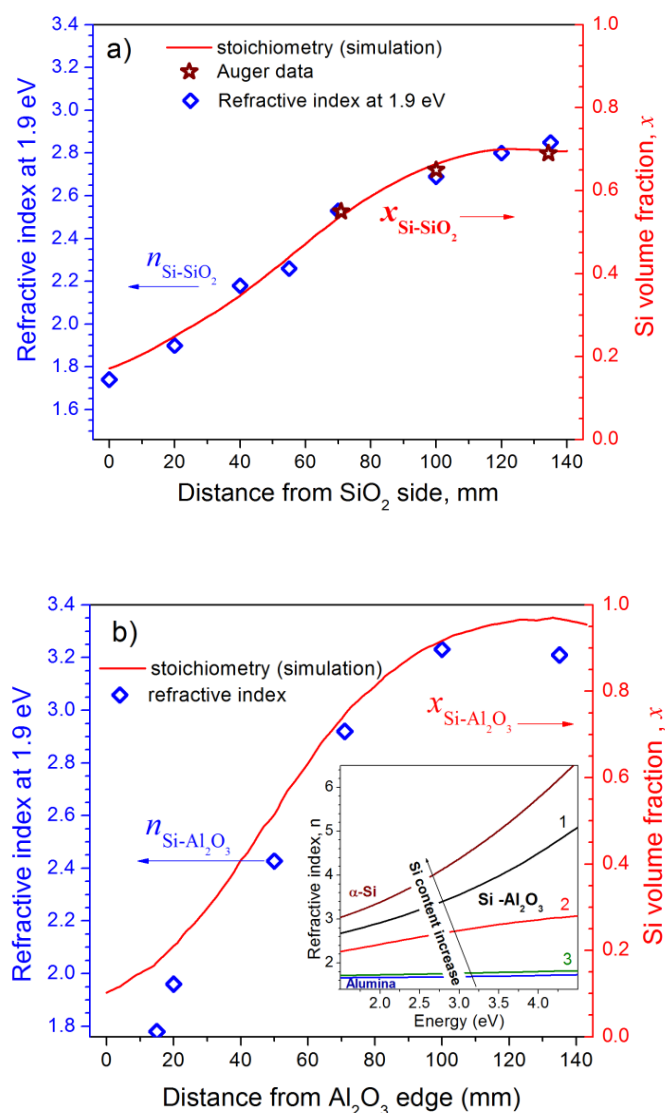


**Figure 3.** a) Variation of  $n_{\text{Si-SiO}_2}$  (diamond-shaped symbols) and  $x_{\text{Si-SiO}_2}$  (taken from Fig. 2a) for Si-SiO<sub>2</sub> film along its length; Auger data (stars) were replotted from Fig. 2a; b) Variation of  $n_{\text{Si-Al}_2\text{O}_3}$  (diamond-shaped symbols) and  $x_{\text{Si-Al}_2\text{O}_3}$  (taken from Fig. 2b) for Si-Al<sub>2</sub>O<sub>3</sub> film. Inset - dispersion relations for amorphous Si, Al<sub>2</sub>O<sub>3</sub>, and Si-Al<sub>2</sub>O<sub>3</sub> films with different  $x = 0.7$  (1), 0.4 (2) and 0.15 (3), reproduced from Ref. [23].

### 3.2. Raman scattering spectra

Raman scattering study showed that as-deposited Si-Al<sub>2</sub>O<sub>3</sub> and Si-SiO<sub>2</sub> films with  $x \geq 0.5$  contained amorphous silicon clusters (a-Si-cl) (Fig.4a). On the other hand, the peak position of the transverse optical (TO) band for Si-Al<sub>2</sub>O<sub>3</sub> films was observed at  $\omega_{\text{TO-a-Si}} = 460 \text{ cm}^{-1}$  contrary to that detected for Si-SiO<sub>2</sub> counterparts at  $\omega_{\text{TO-a-Si}} = 480 \text{ cm}^{-1}$  corresponded to the TO phonon peak position of relaxed amorphous silicon. The shift of the TO phonon observed for Si-Al<sub>2</sub>O<sub>3</sub> samples in comparison with the TO photon band of relaxed amorphous silicon means that a-Si-cl are under elastic stresses. This can be caused by both a-Si-cl/host and film/substrate interfaces due to mismatching in the lattice parameters of the Si phase, the Al<sub>2</sub>O<sub>3</sub> host, and the fused silica substrate.

Taking into account the low-frequency shift observed for Si-Al<sub>2</sub>O<sub>3</sub> samples, one can conclude that these stresses have tensile behavior. It is well known that this effect is negligible for the Si-SiO<sub>2</sub> - films.

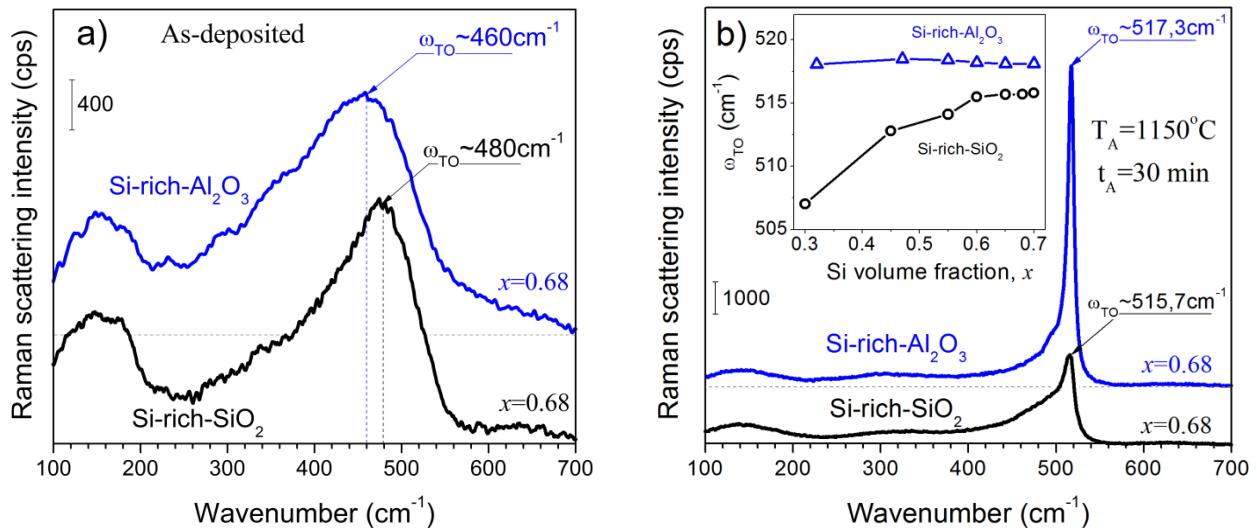


**Figure 4.** Raman scattering spectra of as-deposited (a) and annealed (b) Si-Al<sub>2</sub>O<sub>3</sub> and Si-SiO<sub>2</sub> films with  $x = 0.68$ . The inset in Fig.1b shows the variation of TO phonon band position versus  $x$  for both types of samples. The excitation light energy was 2.54 eV. Note that  $x$  represent  $x_{\text{Si-SiO}_2}$  and  $x_{\text{Si-Al}_2\text{O}_3}$  for the corresponding curves. Reproduced with permission from Ref. [25].

Annealing treatment at  $T_A = 1150$  °C results in the crystallization of the amorphous phase. In the spectra this is accompanied by the decrease of the amorphous bands and the appearance of the crystalline TO phonon band near  $520$  cm<sup>-1</sup>. (Fig.4b). When  $x$  decreases, the shift of the  $\omega_{\text{TO-nc-Si}}$  to lower wavenumbers occurs for Si-SiO<sub>2</sub> (Fig.4b, inset). It is accompanied by its broadening that can be ascribed to the decrease of Si-ncs sizes [40].

In all the Si-Al<sub>2</sub>O<sub>3</sub> samples, the  $\omega_{\text{TO-nc-Si}}$  is shifted to lower wavenumbers ( $517.3$ – $518.7$  cm<sup>-1</sup>) in comparison with the peak position of TO phonon band of bulk Si ( $\omega_{\text{TO-bulk-Si}} = 521$  cm<sup>-1</sup>). However, contrary to Si-SiO<sub>2</sub> films, for Si-Al<sub>2</sub>O<sub>3</sub> samples with  $x = 0.55$ – $0.7$ , only a slight shift of the  $\omega_{\text{TO}}$  towards higher wavenumbers is detected with  $x$  (Fig.4b, inset). It is worth to note that along with the Si crystalline phase, the amorphous Si phase was also detected in annealed samples. However, for the samples with the same  $x$  values its contribution is smaller for the Si-Al<sub>2</sub>O<sub>3</sub> samples in comparison with its Si-SiO<sub>2</sub> counterparts.

### 3.3. XRD patterns

Grazing incidence XRD patterns of annealed Si-SiO<sub>2</sub> and Si-Al<sub>2</sub>O<sub>3</sub> with  $x > 0.5$  are shown in Fig.5a,b. For Si-SiO<sub>2</sub> films we observe wide peaks at  $2\theta \cong 28.5^\circ$  and  $2\theta \cong 95^\circ$  that correspond to the reflection from the (111 and 333) family planes of crystalline Si (Fig. 5a). The absence of any other diffraction peaks can be caused by two factors: (i) small Si-ncs sizes of randomly oriented crystallites and (ii) by the elongated shape of largest crystallites and their partial preferred orientation in  $\langle 111 \rangle$

direction. The latter phenomenon was reported in Ref. [41] and confirmed by an EPR study of similar samples [6]. For Si-Al<sub>2</sub>O<sub>3</sub> films several peaks corresponding to the (111), (220) and (311) Si reflections was detected (Fig.5b). It is seen that these XRD peaks are narrower than those of Si-SiO<sub>2</sub> films. This is an evidence of the larger Si-ncs sizes in Si-Al<sub>2</sub>O<sub>3</sub> films.

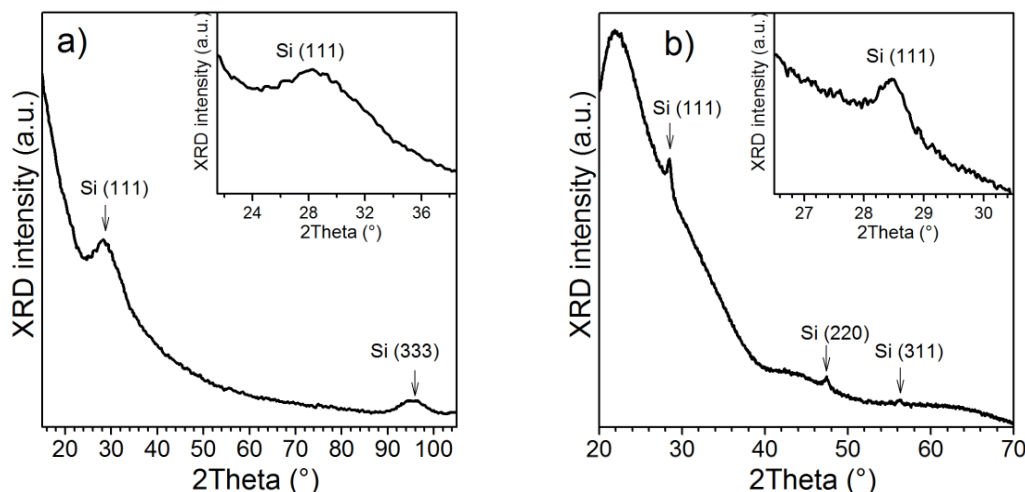


**Figure 5.** Grazing incidence XRD pattern from annealed films: (a) Si-SiO<sub>2</sub> ( $x_{\text{Si-SiO}_2} = 0.6$ ) and (b) Si-Al<sub>2</sub>O<sub>3</sub> ( $x_{\text{Si-Al}_2\text{O}_3} = 0.6$ ). The inset shows the expanded presentation of the (111) Si peak [26].

It turned out that the width of XRD peaks did not vary with  $x$  for  $x > 0.5$ , in the case of Si-Al<sub>2</sub>O<sub>3</sub>, and  $x > 0.6$ , in the case of Si-SiO<sub>2</sub>. Debye-Scherrer formula applied usually for estimation of Si-ncs sizes in the case of grazing geometry gives an overestimated value. It was calculated that the mean size of Si-ncs embedded in Al<sub>2</sub>O<sub>3</sub> and SiO<sub>2</sub> host do not exceed 14 nm and 6 nm, respectively. As shown below the formation of larger Si-ncs in Si-Al<sub>2</sub>O<sub>3</sub> films was confirmed by TEM observation.

### 3.4. TEM observation

High-resolution TEM (HR-TEM) study of the Si-SiO<sub>2</sub> and Si-Al<sub>2</sub>O<sub>3</sub> samples revealed the formation of Si-ncs embedded in the amorphous oxide hosts in both films (Fig.6). The contrast in the HR-TEM images arises from the coherent superposition of the primary and elastically scattered beams. For thin enough imaged area, it is directly connected to the projected atomic structure of the Si-ncs (Fig. 6). It is known that a crystal can be observed in HR-TEM with a significant contrast if it is crystalline, in Bragg orientation with respect to the incident electrons, and if the thickness of the imaged area is not greater than two or three times the diameter of the Si-ncs [42]. Thus, amorphous and mis-oriented particles are excluded from this image. Moreover, thin edges of the Si-ncs are too thin to be imaged as atomic columns. As a consequence, the size of the Si nanocrystals is underestimated. The minimum detectable size that can be measured is equal to about 1.5 nm (i.e.4-5 (110) planes).

HR-TEM images showed that annealing under the same conditions of the Si-SiO<sub>2</sub> and Si-Al<sub>2</sub>O<sub>3</sub> films with the same  $x$  ( $x = 0.6$  in this case) results in the formation of Si-ncs that are larger in Si-Al<sub>2</sub>O<sub>3</sub> films (Fig.6). Their formation is also confirmed by corresponding Fast Fourier Transform

of the images (Fig.6, insets) that clearly demonstrate different rings of randomly oriented Si-ncs.

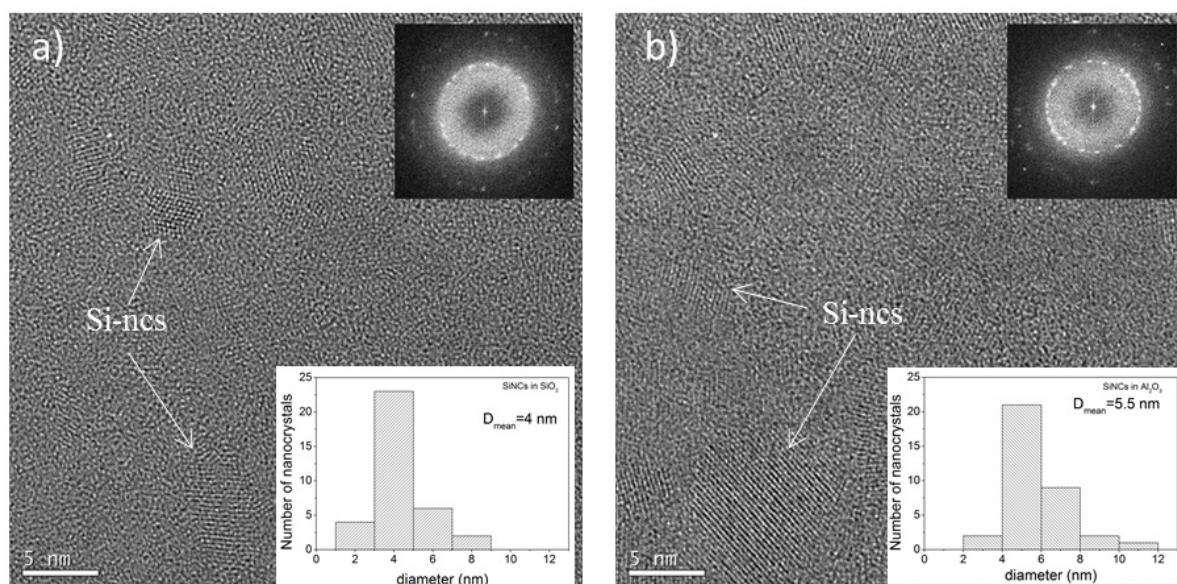


**Figure 6.** High-resolution TEM images for annealed films on cross-sectional specimen: (a) Si-SiO<sub>2</sub> ( $x_{\text{Si-SiO}_2} = 0.6$ ) and (b) Si-Al<sub>2</sub>O<sub>3</sub> ( $x_{\text{Si-Al}_2\text{O}_3} = 0.6$ ). The insets show the associated Fast Fourier Transform of the images and the corresponding size-distributions of Si-ncs.

The average diameters have been extracted from the size-distributions shown in inset of Fig. 6. To build them, 35 nanocrystals have been measured for each sample (on 10 HR-TEM images). When the shape of the domain was not spherical (which is mostly the case), the major axis length has been considered. Touching nanocrystals that would lead to an overestimation of the mean size have been avoided in the statistics. The same has been applied for nanocrystals that are cut at the border of the images. The average diameter as measured by HR-TEM finally represents the size of monocrystalline domains. The Si nanoparticles could be larger and polycrystalline. For this reason, there is no sense to comment on the shape of the size-distribution. However, we can finally conclude that the Si nanocrystals (i.e., monocrystalline domains) are larger when Si nanoparticles are embedded in Al<sub>2</sub>O<sub>3</sub>. They represent the mean size of monocrystalline domains, i.e. Si nanoparticles could be significantly larger and polycrystalline [42]. The number of Si-ncs was found to be higher in Si-Al<sub>2</sub>O<sub>3</sub> than in Si-SiO<sub>2</sub>. The mean diameter of Si-ncs in Si-SiO<sub>2</sub> films is about 4 nm, whereas it exceeds 5.5 nm in Si-Al<sub>2</sub>O<sub>3</sub> film. The discrepancy between the average size measured in the HREM images and the one obtained by XRD for the Si-Al<sub>2</sub>O<sub>3</sub> sample also arises from the increased contribution of the largest nanocrystals in the XRD technique.

### 3.5. Light emitting properties

#### 3.5.1. Si-SiO<sub>2</sub> samples

Usually, no PL emission from as-deposited layers was observed, while after high-temperature annealing a bright emission in visible - near infrared spectral range was detected. PL spectra of the layers with  $x = 0.25$ – $0.5$  measured under 488 nm excitation demonstrate, as a rule, a broad PL (IR-

band) (Fig.7a), which first increases and then decreases with the decrease of  $x$  (Fig.7b, star symbols). Simultaneously the peak position shifts to higher photon energies (Fig.7b, square symbols). This allows attributing that band to exciton recombination in Si nanocrystallites. The increase of the PL intensity can be attributed to the increase of the emission probability with decreasing crystallite size as well as to the higher light penetration in the sample, while the PL intensity decrease can be assigned to the decrease of the number of Si-ncs in the sample. On the other hand, when  $x = 0.25$ – $0.3$ , additional contribution of a defect related band can be found in PL spectra [5].

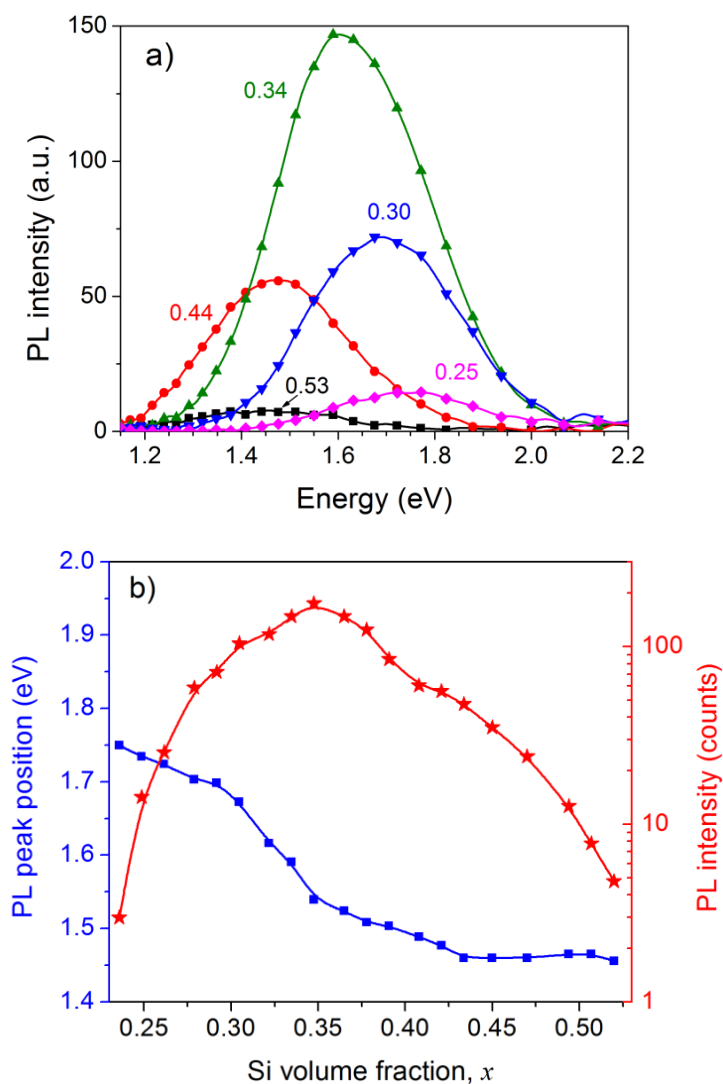


**Figure 7.** a) PL spectra of Si-SiO<sub>2</sub> films with different Si volume fractions mentioned in the figure. Excitation energy is 2.54 eV; b) Dependence of PL intensity (star symbols) and PL peak position (square symbols) of Si-SiO<sub>2</sub> films on Si volume fraction. Reproduced from Ref. [26].

The PL emission of Si-SiO<sub>2</sub> samples was also investigated under ultraviolet (337 nm, 3.68 eV) excitation. Contrary to the former case, several PL bands can be observed (Fig.8a). The dependence of their peak positions on  $x$  is shown in Fig.8b. It is seen that the peak position of IR band shifts to higher energies with the decrease of  $x$ , while the peak positions of other bands do not shift in the

Si-rich and Si-poor regions. It should be noted that in the intermediate region ( $0.3 < x < 0.5$ ) the peak position is determined by overlapping of different bands (Fig.8a,b). Therefore, the IR-band can be due to exciton recombination in Si-ncs, while other bands can be ascribed to carrier recombination through defects on Si-nc/matrix interface or through defects in the matrix. These can be referred to as R-band (at  $\sim 1.7$  eV), O-band (at  $\sim 2.05$ ) and G-band (at  $\sim 2.35$  eV) (Fig.8b). In the following we suggest that these defects are silicon oxide defects: (i) the intensities of these bands continue to increase with increasing SiO<sub>2</sub> content while the intensity of Si-ncs related band already decreases (Fig. 8b); (ii) the O-band was observed also in silica optical fibers [43,44] as well as in ion implanted SiO<sub>2</sub> films [45] and was attributed to non-bridging oxygen hole centers [46,47]; (iii) the G-bands were observed in silicate glass (Fig. 8a), in Si-ion-implanted SiO<sub>2</sub> films [48] and in porous silicon [49]; (iv) in contrast to the IR-band the O- and G-bands do not disappear at the Si-poor end in spite of a sharp drop in their intensities at  $x < 0.28$ .

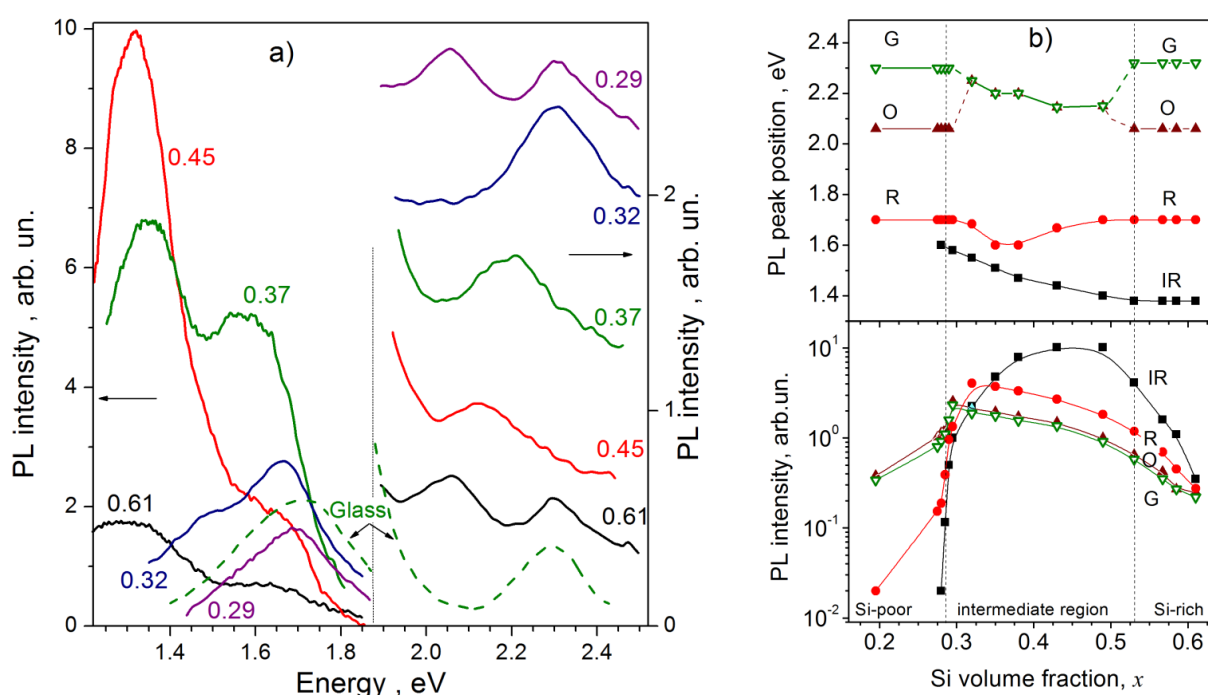


**Figure 8.** a) PL spectra of the Si-SiO<sub>2</sub> films with different composition ( $x = 0.61, 0.45, 0.37, 0.32, 0.29$ ). Excitation energy is 3.68 eV; PL spectrum of the glass is shown by dashed curve for comparison. b) Dependence of PL intensity and PL peak position of different bands (infrared (IR), red (R), orange (O) and green (G)) on the Si volume fraction  $x$ . Reproduced from Ref. [5] with permission of Elsevier publisher.

It should be noted that IR-band independently on wavelength of excitation light is most intense. Thus, the main recombination channel in Si-SiO<sub>2</sub> films is exciton recombination in Si-ncs.

### 3.5.2. Si-Al<sub>2</sub>O<sub>3</sub> films

PL emission from as-deposited samples was not detected for  $x > 0.5$ , whereas for  $x < 0.5$  only the peak at  $\sim 560$  nm (2.21 eV) was observed (not shown here). It was found to be similar to that detected in pure Al<sub>2</sub>O<sub>3</sub> film and assigned to F<sub>2</sub><sup>2+</sup> centers [50].

Both CA and RTA treatments yield visible PL emission in wider spectral range. Figure 9 represents the PL spectra of annealed samples after CA treatment as measured at 300 K. These spectra contain two broad PL bands, whose maxima are observed at 575–600 nm (2.06–2.15 eV) and 700–750 nm (1.65–1.77 eV) accompanied by near-infrared tail (or weak band at 1.55–1.6 eV). These bands can be well-separated (for  $x = 0.45$ – $0.5$ ) or strongly overlapped. The first band consists of two components with maxima at  $\sim 2.06$  eV and  $\sim 2.18$  eV. The latter one is clearly seen in the sample with  $x = 0.3$  being similar to PL emission from  $F_2^{2+}$  centers in  $Al_2O_3$  [24]. At the same time, both emission components are strongly overlapped in the samples with  $x > 0.3$  (Fig. 9).

To elucidate the origin of PL emission from the films investigated, the PL spectra were measured also at 80 K (Fig.10). It should be expected that peak position and intensity of the PL bands related to defects in oxide matrixes will not change under cooling down to 80 K because of deep level related intra-defect transition. In fact, most oxide defects demonstrate such PL behavior in the 80–300 K range.

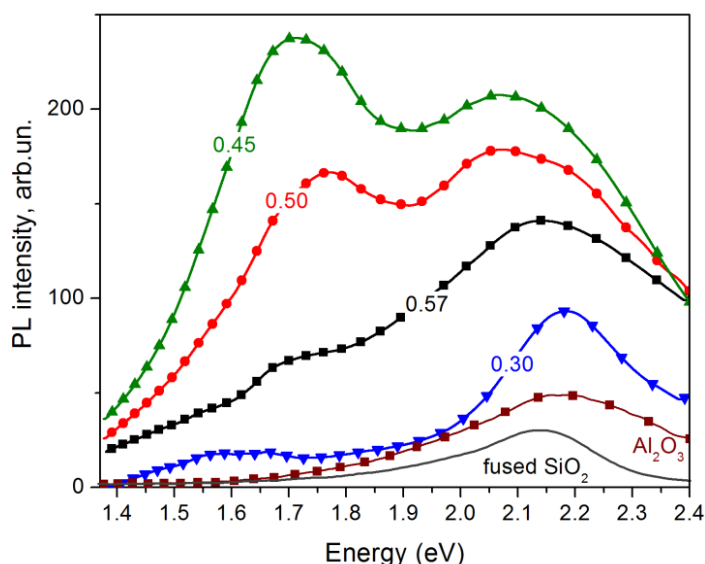


**Figure 9.** PL spectra of the samples with different  $x$  values submitted to conventional annealing at 1150 °C for 30 min in  $N_2$  flow. The  $x$  values are shown in the figure. The spectrum of pure  $Al_2O_3$  and fused  $SiO_2$  substrate are also shown. Excitation light energy is 2.54 eV. Reproduced from Ref.[23].

Figure 10 presents the comparison of the PL properties of the samples after CA and RTA treatments measured at 300 and 80 K.

As shown in Fig.10a such a behavior is observed for the PL band at 575–600 nm (2.06–2.15 eV) that allows its ascribing to defects. A similar band was observed in Si-rich- $Al_2O_3$  materials [51,52] as well as in Si-rich- $SiO_2$  samples [5]. In the former case it was ascribed to F-like centers in  $Al_2O_3$ , whereas in the latter case to  $E'$  and NBOHC defects in  $SiO_2$ . Thus, this emission can be ascribed to the defects located near Si-ncs/host interface (i.e. in the oxide shell covered these Si-ncs). This shell can consist of both alumina and silica [19,22].

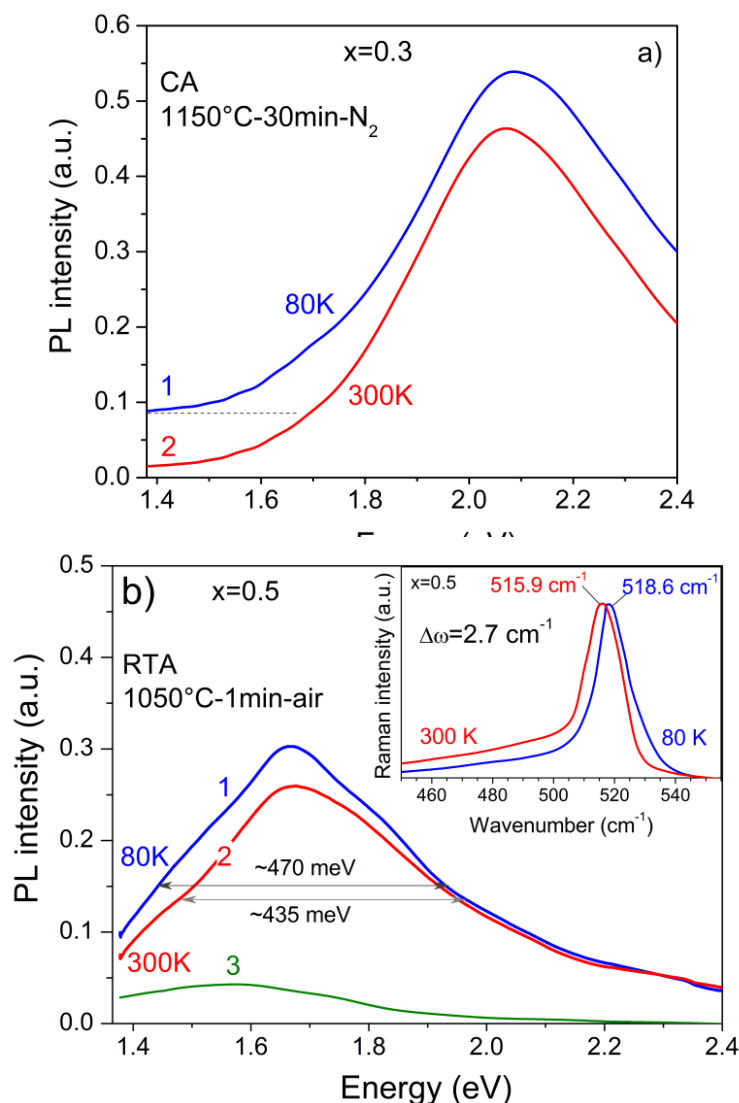


**Figure 10.** PL spectra of Si-Al<sub>2</sub>O<sub>3</sub> samples submitted to the conventional annealing (CA) at 1150 °C for 30 min (a) and rapid thermal annealing (RTA) at 1050 °C for 1 min (b). The excitation energy was 3.8 eV for both figures. The Si contents were  $x = 0.3$  (a) and 0.5 (b) and the temperatures of the measurements were 80 K (curves 1) and 300 K (curves 2). Curve 3 in Fig. b) represents the difference of curves 1 and 2. The spectra in (a) are vertically shifted for clarity. Inset in b) shows Raman scattering spectra as measured with a 2.54 eV excitation taken at 80K and 300K. Reproduced from Ref. [23].

In contrast with the above, the PL band that is related to exciton recombination in quantum confinement Si-ncs, has to demonstrate a shift of its peak position to higher energies due to Si band-gap increase [53,54] and an increase of PL intensity [6]. It should be noted that for Si-SiO<sub>2</sub> films the temperature dependence of PL peak position was found to be similar to silicon bandgap variation for  $x > 0.5$  testifying the exciton nature of the observed. However, for Si-Al<sub>2</sub>O<sub>3</sub> films, the appearance of strain (either tensile or compressive) results in the decrease of Si-ncs bandgap [55] that should reduce the blue-shift of the PL peak position with cooling.

The investigation of Raman scattering spectra at low temperature shows that peak position of

Si-ncs related TO phonon is blue shifted by about  $2.7 \text{ cm}^{-1}$  (Fig.10,b,inset). At the same time, for bulk Si this shift is about  $4.5 \text{ cm}^{-1}$  [56]. This means that the cooling results in an increase of tensile stress in the Si-ncs. Such stresses are due to the difference in thermal expansion coefficients of  $\text{Al}_2\text{O}_3$  ( $5.4 \times 10^{-6}/\text{K}$ ), Si ( $3 \times 10^{-6}/\text{K}$ ) and the  $\text{SiO}_2$  ( $0.77\text{--}1.4 \times 10^{-6}/\text{K}$ ). In particular, with cooling  $\text{Al}_2\text{O}_3$  will compress much more than  $\text{SiO}_2$ . Thus,  $\text{SiO}_2$  substrate will stretch  $\text{Al}_2\text{O}_3$  film and additional tensile stress in  $\text{Al}_2\text{O}_3$  will appear under cooling.

At the same time, the  $\text{Al}_2\text{O}_3$  host compresses the Si-ncs. Based on Raman scattering data we estimated the relative deformation in the Si-nc under cooling, using the approach of Ref. [52] and we found biaxial tensile strain of about 0.15%. Taking into account the results of Ref. [57], one can appreciate that such a strain can cause the narrowing of Si bandgap by 22 meV. Thus, as a consequence, the shift of the peak position of Si-ncs related PL band has to be about 19 meV only. Such a shift for the broad featureless PL bands, observed in our experiment, can be negligible. Therefore, we focus now on the variation of the PL intensity.

The shape of the PL band with the maximum at about 700–750 nm (1.77–1.65 eV) and its temperature behavior, which was investigated for the sample after rapid annealing (RTA) are more complicated. Its peak position is also independent on temperature and the intensity of short-wavelength wing (500–650 nm (2.06–2.15 eV)) does not change with cooling (Fig.10b). On the other hand, a broadening of PL band towards longer wavelengths and a slight increase of its intensity at the maximum is observed. The independence of the intensity of the short-wavelength wing allows ascribing of PL component at 500–650 nm (2.06–2.15 eV) to the radiative recombination of carriers via host defects.

Since this PL spectrum is complex and contains several overlapping components with very weak features, the deconvolution of PL spectrum on the components cannot be performed. Thus, we used the subtraction of the PL spectrum detected at 300 K from that measured at 80 K. It is seen, that with cooling (Fig.10b, curve 3) an increase of the intensity of the PL component in the 780–900 nm spectral range, takes place. The most probable reason for this increase is the rise of the contribution of carrier recombination in Si-ncs to the PL spectrum. This is in agreement with the data of Ref. [20], obtained on the samples prepared by ion implantation. At the same time the PL component at 700–750 nm (1.77–1.65 eV) can be probably attributed to the defects located in matrix near Si-nc/matrix interface because the intensity does not practically change with temperature. In fact, a slight increase of the PL intensity in its maximum appears to be due to overlapping with the near-infrared component, the intensity of which increases with cooling.

Based on the PL results, one can conclude that the main contribution to the PL spectra in our samples is given by the carrier recombination through different defects located near Si-nc/matrix interface (for instance, oxygen vacancies in  $\text{Al}_2\text{O}_3$ ). On the other hand the near-IR PL band is due to exciton recombination in Si-ncs. The high concentration of interface and matrix defect (in particular, the high intensity of PL band at 700–750 nm) obviously hinders the observation of exciton recombination.

The information on interface defects as well as the presence of the amorphous phase can be extracted from EPR measurements.

### 3.6. EPR study

The EPR spectra of as-deposited samples of the both types' with  $x \geq 0.3$  are dominated by the signal with  $g_1 = 2.0055$  (Fig.11) that corresponds to the silicon dangling bonds (Si DB) and testifies to

the presence of an amorphous Si phase. Its intensity reflects the total number of these centers which decreases with the decrease of  $x$ . The dangling bond concentration that we estimated from the EPR spectra for the samples with  $x = 0.7$  is higher for Si-Al<sub>2</sub>O<sub>3</sub> ( $\sim 10^{19}$  centers/cm<sup>3</sup>) than for Si-SiO<sub>2</sub> ( $\sim 10^{18}$  centers/cm<sup>3</sup>).

For the Si-SiO<sub>2</sub> with  $x \leq 0.45$  we have observed the appearance of an anisotropic signal with  $g_2 = 2.0018$  (Fig. 11b). The  $g$ -factor of this signal was determined as the intersection of the EPR signal with the zero-line. With decreasing  $x$  the intensity of this anisotropic signal increases at first and then decreases (not shown here). Such dependence could mean that the corresponding EPR center is connected with both the silicon oxide and the silicon phases. In this case the increase of the intensity is due to the increase of silicon oxide volume, while the decrease is caused by the decrease of Si content. This conclusion is in agreement with the absence of this anisotropic signal in films deposited from the silicon oxide target only. This signal is similar to the one observed for milled quartz, but its nature needs additional study.

Annealing treatment resulted in the transformation of the EPR spectra of both types (Si-SiO<sub>2</sub> and Si-Al<sub>2</sub>O<sub>3</sub>) of samples. In Si-SiO<sub>2</sub> films with  $x > 0.3$ , the intensity of an asymmetric signal with  $g_3 = 2.0062$ , while increasing with  $x$  (Fig. 11a), was found to be slightly lower than that of the Si DB related centers. Asymmetric shape of this signal and the shift of  $g$ -factor to higher values as well as the decrease of its intensity in comparison with that of as-deposited samples, allows us to assign it to the superposition of the signals due to the Si DB and P<sub>b</sub>-like centers that appear when the Si-ncs are formed [6]. For  $x < 0.45$ , an isotropic signal with  $g_4 = 2.0028$  and a peak-to-peak width  $\Delta H \sim 3.5$  G appeared instead of the anisotropic one with  $g_2 = 2.0018$ . Its intensity, first, increases and then decreases with the decrease of  $x$ . The highest amplitude of this signal is observed for samples with  $x = 0.22$  (Fig. 11c). The signal with  $g_4 = 2.0028$  was also observed for oxidized silicon annealed additionally in oxygen-free ambient at 960-1130°C and was ascribed to S-centers, previously assigned to E'-like defects of O<sub>2</sub>Si≡Si• and/or OSi<sub>2</sub>≡Si• types [58]. This is excess-Si defect in the SiO<sub>2</sub> matrix that can be considered as a signal of non-stoichiometric silicon oxide. It is obvious that such defects can be built by excess Si atoms which cannot form Si-ncs due to their low concentration. Similar behavior of the intensities of signals with  $g_4 = 2.0028$  (annealed samples) and  $g_2 = 2.0018$  (as-deposited ones) versus  $x$  allows us to assume that the former signal appears due to the transformation of the latter case.

Instead of single one with  $g_1 = 2.0055$  detected for as-deposited films, annealed Si-Al<sub>2</sub>O<sub>3</sub> samples showed two signals with  $g_5 = 2.0068$  and  $g_6 = 2.0027$  (Fig. 11b). The first of these signals dominates for the samples with  $x \geq 0.4$ , while the other one is observed at  $x < 0.4$ . The signal with  $g_5 = 2.0068$  can be attributed to the superposition of Si dangling bonds and P<sub>b</sub>-like centers that can be a feature of both the Si/SiO<sub>2</sub> and Si/Al<sub>2</sub>O<sub>3</sub> interfaces [59]. The higher value of  $g_5$ -factor in comparison with  $g_3$ -one (2.0068 vs. 2.0062) and the decrease of EPR signal intensity after annealing in comparison with corresponding signal in Si<sub>x</sub>(SiO<sub>2</sub>)<sub>1-x</sub> samples, suggests that in the case of Si<sub>x</sub>(Al<sub>2</sub>O<sub>3</sub>)<sub>1-x</sub> films the contribution of the DB to the signal is lower.

Since the  $g_6 = 2.0027$  observed for annealed Si-Al<sub>2</sub>O<sub>3</sub> is close to the  $g_4 = 2.0028$  of the corresponding Si-SiO<sub>2</sub> samples and both signals have similar peak-to-peak widths ( $\sim 4.0$  G vs.  $\sim 3.5$  G), it can be concluded that the center with  $g_6 = 2.0027$  in Si-Al<sub>2</sub>O<sub>3</sub> is similar to S-centers observed in Si-SiO<sub>2</sub> samples with  $x < 0.45$  (which is characteristics of non-stoichiometric silicon oxide). The dependence of its intensity on  $x$  (Fig. 11f) is also similar to one that we obtained for the Si-SiO<sub>2</sub> films (Fig. 11c).

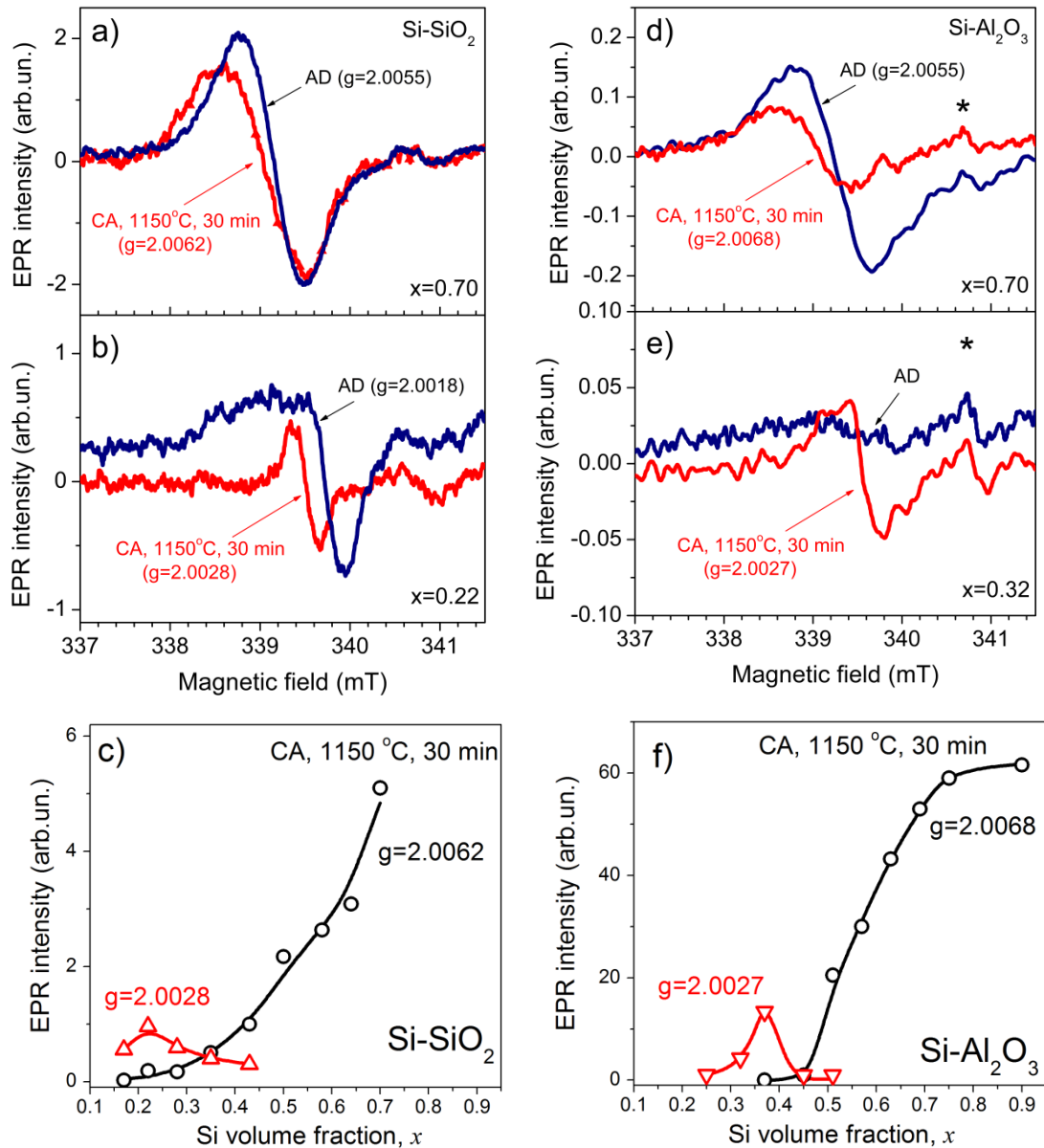


**Figure 11.** EPR data for Si-SiO<sub>2</sub> (a-c) and Si-Al<sub>2</sub>O<sub>3</sub> (d-f) samples with  $x = 0.70$  (a, d), 0.32 (e) and 0.22 (b). EPR spectra for Si-SiO<sub>2</sub> (a,b) and Si-Al<sub>2</sub>O<sub>3</sub> (d,e) measured on as-deposited (AD) and annealed samples; c), f) dependence of integrated intensities of two main EPR signals versus  $x$  for Si-SiO<sub>2</sub> (c) and Si-Al<sub>2</sub>O<sub>3</sub> (f). The signal of the superfine component of MgO:Cr<sup>3+</sup> reference is shown by star symbols. Reproduced with permission from Ref. [25].

#### 4. Discussion

The comparison of the above reported results allows us to reveal the common and different features of the two types of films that we studied.

Our investigation of the structural properties of as-deposited Si-SiO<sub>2</sub> and Si-Al<sub>2</sub>O<sub>3</sub> films showed that one of their common features is the presence of an amorphous Si phase. This phase is detected by

the Raman scattering method for the samples with  $x > 0.45$ , whereas EPR data confirms the presence of this phase in the samples with  $x > 0.3$  that is due to higher sensitivity EPR method there.

As deposited Si-Al<sub>2</sub>O<sub>3</sub> films were found, contrary to the Si-SiO<sub>2</sub> films, to be stressed. These stresses are tensile and are caused by the mismatching in the lattice constants of fused silica substrate and the deposited Si-Al<sub>2</sub>O<sub>3</sub> film as well as Si clusters and oxide host.

Comparison of XRD and Raman scattering data shows that after annealing treatment the Si-ncs in Si<sub>x</sub>(Al<sub>2</sub>O<sub>3</sub>)<sub>1-x</sub> samples are also stressed. In fact, the peak position of the TO phonon band of the Si-ncs for the samples with  $x > 0.5$  is shifted to the lower frequencies ( $\omega_{\text{TO-nc-Si}} = 517\text{--}518 \text{ cm}^{-1}$ ) in comparison with that for bulk Si ( $\omega_{\text{TO-bulk-Si}} = 521 \text{ cm}^{-1}$ ). The mean size of Si-ncs was estimated from the XRD data to be about 14 nm. It is obvious that the contribution of phonon quantum confinement effect is negligible in this case. This means that the Si-ncs in the Si-Al<sub>2</sub>O<sub>3</sub> samples are under tensile stress contrary to the Si-ncs in the Si-SiO<sub>2</sub> films.

As mentioned above, the peak position of the Raman band of the Si-ncs in Si-Al<sub>2</sub>O<sub>3</sub> for samples of  $x = 0.6$  shifts slightly to high frequencies with the decrease of  $x$ . This shift cannot be caused by the change of the crystallites' size because the decrease of Si content should result in the decrease of Si crystallites and lead to the opposite shift of Raman line. The observed shift is obviously caused by the decrease of amorphous Si phase content that is in agreement with the decrease of the intensity of the TA phonon band of amorphous Si ( $\omega_{\text{TA-a-Si}} = 150 \text{ cm}^{-1}$ ) and EPR data. Thus, the sizes of Si-ncs in Si-Al<sub>2</sub>O<sub>3</sub> films cannot be estimated from the Raman data.

Another situation occurs in the Si-SiO<sub>2</sub> films. With the decrease of  $x$  there is a shift of  $\omega_{\text{TO-nc-Si}}$  to lower wavenumbers (Fig.1b, inset) and this is accompanied by the increase of full-width at half maximum of this phonon band (not shown here). The sizes of Si-ncs embedded in SiO<sub>2</sub> host can be estimated from the fitting of Raman scattering spectra. Based on such analysis we found that the increase of the Si-ncs mean size from  $\sim 2.7$  nm to 6.0 nm takes place in the Si-SiO<sub>2</sub> samples when  $x$  increases from 0.3 to 0.5, whereas for  $x > 0.5$ , the Si-ncs size does not change practically. These results are in a good agreement with our XRD data.

The results that we obtained showed that the mean size of Si-ncs in Al<sub>2</sub>O<sub>3</sub> exceeds that for Si-ncs in SiO<sub>2</sub> for the films with same  $x$  values. One of the reasons of this phenomenon can be faster diffusion of Si in alumina than that in silica in the case when Si-ncs formation is driven by Si diffusion towards Si-nuclei that is a diffusion-limited growth phenomena [24,42]. Another reason for that can be the lower temperature required for phase separation in Si-Al<sub>2</sub>O<sub>3</sub> than that for Si-SiO<sub>2</sub>. In spite of that difference, both types of films have here one common feature. For the samples with  $x > 0.5$  the mean Si-ncs sizes do not change with  $x$ . This can be connected with presence of amorphous Si inclusions in the as-deposited films. In this case their crystallization can contribute to appearance of Si-nc in addition to the process of phase separation. For  $x > 0.5$  this contribution can be crucial. The larger size of Si-ncs in the Al<sub>2</sub>O<sub>3</sub> host, in this case, is obviously due to the influence of Al which promotes the lowering of Si crystallization temperature [60].

Our Raman scattering spectra of annealed films showed also a relatively higher contribution of the amorphous Si phase in the as-deposited Si-SiO<sub>2</sub> than in the Si-Al<sub>2</sub>O<sub>3</sub> films. This is in agreement of EPR data. In fact, higher contribution of Si DB signal in EPR spectra of the Si-SiO<sub>2</sub> samples is obviously caused by the higher contribution of amorphous Si phase. Our Raman scattering and EPR data show that after annealing the contribution of the amorphous phase is higher in Si-SiO<sub>2</sub> films. This is in agreement with the above conclusion that presence of Al results in the lowering of Si crystallization temperature.

Our study enables to underline that in the Si-Al<sub>2</sub>O<sub>3</sub> samples with low  $x$  values the EPR signal, which is characteristic of non-stoichiometric silicon oxide, is observed. Since this signal appears under thermal treatment, we can conclude that silicon suboxide phase is formed under the phase separation process.

Our results show significant difference in the PL properties of Si-SiO<sub>2</sub> and Si-Al<sub>2</sub>O<sub>3</sub> films. For Si-SiO<sub>2</sub> films the dominant recombination channel is exciton recombination in the Si-ncs. In contrast, the PL spectra of Si-Al<sub>2</sub>O<sub>3</sub> films are dominated by several PL bands caused by recombination of carriers through the defects of matrix near Si-ncs/host interface. On the other hand, the contribution the band which can be ascribed to exciton recombination in the Si-ncs is relatively weak.

This can be due to high number of non-radiative defects at Si-ncs/Al<sub>2</sub>O<sub>3</sub> interface which, in particular, can appear due to mechanical stress in Si-Al<sub>2</sub>O<sub>3</sub> films. These non-radiative centers can be P<sub>b</sub>-like centers. Our EPR data allow concluding that the concentration of these defects is larger in Si-Al<sub>2</sub>O<sub>3</sub> samples than in the Si-SiO<sub>2</sub> films with the same  $x$  values. In fact, the pronounced shift of the  $g$ -factor in annealed samples is the evidence that the contributions of both P<sub>b</sub>-like centers and Si DB in EPR spectra are comparable.

It should be noted that the defect-related bands in Si-Al<sub>2</sub>O<sub>3</sub> films can also be attributed to F-like centers in Al<sub>2</sub>O<sub>3</sub> (found at ~2.15 eV and ~2.19 eV) [50,52]. It is also worth to note that PL components at ~1.65–1.77 eV and ~2.06 eV were observed only when Si-ncs are present in the film. This can be explained by their location near Si-ncs or at Si-ncs/host interface.

## 5. Conclusions

In this paper we have made a comparison of the structural and luminescence properties of Si-SiO<sub>2</sub> and Si-Al<sub>2</sub>O<sub>3</sub> films with different Si content that we have studied in the last few years. These films were fabricated by using magnetron sputtering onto quartz substrates. The formation of amorphous Si clusters upon the deposition process was observed in both types of films for the samples with  $x > 0.3$ . The annealing treatment at 1150 °C during 30 min resulted in the formation of Si nanocrystallites (Si-ncs). Because of the presence of amorphous Si inclusions in the as-deposited films two processes were found to contribute to their formation: the crystallization of existing inclusions and the process of phase separation at high temperatures. The first process can be responsible for independence of mean sizes of crystallites for  $x > 0.5$  that was observed in the both types of annealed films. On the other hand, many differences were found in structural and photoluminescence properties of these films. The Si-nc sizes were found to be larger in Si-Al<sub>2</sub>O<sub>3</sub> films than that in Si-SiO<sub>2</sub> counterparts with the same  $x$  values. This can be caused by faster diffusion of Si in alumina than in silica or by lower temperature required for phase separation or for Si crystallization in Si-Al<sub>2</sub>O<sub>3</sub> in comparison with that of Si-SiO<sub>2</sub>. The latter is in agreement with Raman scattering and EPR spectra of annealed films which show the relatively higher contribution of amorphous Si phase in the Si-SiO<sub>2</sub> in comparison with that of Si-Al<sub>2</sub>O<sub>3</sub>. In addition, the presence of tensile stress in Si-nc embedded in Si-Al<sub>2</sub>O<sub>3</sub> films is observed that is due to mismatching between the lattice parameters of the Si phase, the Al<sub>2</sub>O<sub>3</sub> host and the fused silica substrate. It is shown that exciton recombination in Si-ncs is dominant radiative channel in Si-SiO<sub>2</sub> films while the emission from the oxide defects is the dominant mechanism in the Si-Al<sub>2</sub>O<sub>3</sub> films. This is attributed to the high number of non-radiative defects at the Si-ncs/Al<sub>2</sub>O<sub>3</sub> interface that follows the mechanical stress in Si-Al<sub>2</sub>O<sub>3</sub> films.

## Acknowledgments

This work was partly supported by the Programme Investissements d'Avenir of the program ANR-11-IDEX-0002-02, ref. ANR-10-LABX-0037-NEXT (grant for invited researchers) as well as by bilateral Ukrainian-French program DNIPRO (2015-2016 edition), as well as National academy of sciences of Ukraine (project III-4-16). The research leading to these results has received funding from the European Union Seventh Framework Programme under Grant Agreement 312483-ESTEEM2 (Integrated Infrastructure Initiative–I3). The figures 3b (inset) and 10a,b were reproduced here from their original publication in Ref. [23] following the permission of the Springer publisher.

## Conflict of Interest

All authors declare no conflict of interest in this paper.

## References

1. Canham LT (1990) Silicon quantum wire array fabrication by electrochemical and chemical dissolution of wafers. *Appl Phys Lett* 57: 1046–1048.
2. Lehman V, Gosele U (1991) Porous silicon formation: A quantum wire effect. *Appl Phys Lett* 58: 856–858.
3. Shimizu-Iwayama T, Nakao S, Saitoh K (1994) Visible photoluminescence in Si<sup>+</sup>-implanted thermal oxide films on crystalline Si. *Appl Phys Lett* 65: 1814–1816.
4. Chen XY, Lu YF, Tang LJ, et al. (2005) Annealing and oxidation of silicon oxide films prepared by plasma-enhanced chemical vapor deposition. *J Appl Phys* 97: 014913.
5. Khomenkova L, Korsunskaya N, Yukhimchuk V, et al. (2003) Nature of visible luminescence and its excitation in Si-SiO<sub>x</sub> systems. *J Lumin* 102/103: 705–711.
6. Baran N, Bulakh B, Venger Ye, et al. (2009) The structure of Si-SiO<sub>2</sub> layers with high excess Si content prepared by magnetron sputtering. *Thin Solid Films* 517: 5468–5473.
7. Khomenkova L, Korsunskaya N, Baran M, et al. (2009) Structural and light emission properties of silicon-based nanostructures with high excess silicon content. *Physica E* 41: 1015–1018.
8. Qin GG, Liu XS, Ma SY, et al. (1997) Photoluminescence mechanism for blue-light-emitting porous silicon. *Phys Rev B* 55:12876–12879.
9. Khomenkova L, Korsunskaya N, Torchynska T, et al. (2002) Defect-related luminescence of Si/SiO<sub>2</sub> layers. *J Phys Condens Matter* 14:13217–13221.
10. Sa'ar A (2009) Photoluminescence from silicon nanostructures: The mutual role of quantum confinement and surface chemistry. *J Nanophotonix* 3: 032501 (56 pages).
11. Balberg I (2011) Electrical transport mechanisms in three dimensional ensembles of silicon quantum dots. *J Appl Phys* 110: 061301 (26 pages).
12. Koshida N (2009) Device Applications of Silicon Nanocrystals and Nanostructures, Springer, 344 p.
13. Jamal Deen M, Basu P K (2012) Silicon Photonics: Fundamentals and Devices, Wiley, 192 p.
14. Khomenkova L, Portier X, Cardin J, et al. (2010) Thermal stability of high-*k* Si-rich HfO<sub>2</sub> layers grown by RF magnetron sputtering. *Nanotechnology* 21: 285707 (10 pages).

15. Steimle RF, Muralidhar R, Rao R, et al. (2007) Silicon nanocrystal non-volatile memory for embedded memory scaling. *Microelectronics Reliability* 47:585–592.
16. Baron T, Fernandes A, Damlencourt JF, et al. (2003) Growth of Si nanocrystals on alumina and integration in memory devices. *Appl Phys Lett* 82: 4151–4153.
17. Pillonnet-Minardi A, Marty O, Bovier C, et al. (2001) Optical and structural analysis of  $\text{Eu}^{3+}$ -doped alumina planar waveguides elaborated by the sol–gel process, *Optical Materials* 16: 9–13.
18. Kenyon AJ (2002) Recent developments in rare-earth doped materials for optoelectronics. *Progress in Quantum Electronics* 26: 225–284
19. Mikhaylov AN, Belov AI, Kostyuk AB, et al. (2012) Peculiarities of the formation and properties of light-emitting structures based on ion-synthesized silicon nanocrystals in  $\text{SiO}_2$  and  $\text{Al}_2\text{O}_3$  matrices. *Physics of the Solid State* (St.Petersburg, Russia) 54: 368–382.
20. Yerci S, Serincan U, Dogan I, et al. (2006) Formation of silicon nanocrystals in sapphire by ion implantation and the origin of visible photoluminescence. *J Appl Phys* 100: 074301 (5 pages).
21. Núñez-Sánchez S, Serna R, García López J, et al. (2009) Tuning the  $\text{Er}^{3+}$  sensitization by Si nanoparticles in nanostructured as-grown  $\text{Al}_2\text{O}_3$  films. *J Appl Phys* 105: 013118 (5 pages).
22. Bi L, Feng JY (2006) Nanocrystal and interface defects related photoluminescence in silicon-rich  $\text{Al}_2\text{O}_3$  films. *J Lumin* 121:95–101.
23. Korsunska N, Khomenkova L, Kolomys O, et al. (2013) Si-rich  $\text{Al}_2\text{O}_3$  films grown by RF magnetron sputtering: structural and photoluminescence properties versus annealing treatment. *Nanoscale Res Lett* 8: 273.
24. Korsunska N, Stara T, Strelchuk V, et al. (2013) The influence of annealing on structural and photoluminescence properties of silicon-rich  $\text{Al}_2\text{O}_3$  films prepared by co-sputtering. *Physica E* 51: 115–119.
25. Khomenkova L, Kolomys O, Baran M, et al. (2014) Structure and light emission of Si-rich  $\text{Al}_2\text{O}_3$  and Si-rich  $\text{SiO}_2$  nanocomposites. *Microelectr Eng.* 125: 62–67.
26. Khomenkova L, Kolomys O, Baran M, et al. (2014) Comparative investigation of structural and optical properties of Si-rich oxide films fabricated by magnetron sputtering. *Adv Mat Res* 854: 117–124.
27. HORIBA: Spectroscopic Ellipsometry, DeltaPsi2 Software Platform. <http://www.horiba.com/scientific/products/ellipsometers/software/>
28. Hanak JJ (1970) The "Multiple-Sample Concept" in Materials Research: Synthesis, Compositional Analysis and Testing of Entire Multicomponent Systems. *J Mater Sci* 5: 964–971.
29. Abeles B, Sheng P, Coutts MD, et al. (1975) Structural and electrical properties of granular metal films. *Adv Phys* 24: 407–461.
30. Farooq M, Lee ZH (2002) Optimization of the sputtering process for depositing composite thin films. *J Korean Phys Soc* 40: 511–516.
31. Khomenkova L, Korsunska N, Sheinkman M, et al. (2007) Chemical composition and light emission properties of Si-rich- $\text{SiO}_x$  layers prepared by magnetron sputtering. *Semicond Phys Quantum Electron Optoelectron* 10: 21–25.
32. Charvet S, Madelon R, Goubilleau F, et al. (1999) Spectroscopic ellipsometry analyses of sputtered Si/ $\text{SiO}_2$  nanostructures. *J Appl Phys* 85: 4032 (8 pages).
33. Buiu O, Davey W, Lu Y, et al. (2008) Ellipsometric analysis of mixed metal oxides thin films. *Thin Solid Films* 517: 453–455.
34. Forouhi AR, Bloomer I (1986) Optical dispersion relations for amorphous semiconductors and

- amorphous dielectrics. *Phys Rev B* 34: 7018–7026.
35. Jelisson GE Jr, Modine FA (1996) Parameterization of the optical functions of amorphous materials in the interband region. *Appl Phys Lett* 69: 371–373.
  36. Serenyi M, Lohner T, Petrik P, et al. (2007) Comparative analysis of amorphous silicon and silicon nitride multilayer by spectroscopic ellipsometry and transmission electron microscopy. *Thin Solid Films* 515: 3559–3562.
  37. Houska J, Blazek J, Rezek J, et al. (2012) Overview of optical properties of Al<sub>2</sub>O<sub>3</sub> films prepared by various techniques. *Thin Solid Films* 520: 5405–5408.
  38. Bruggeman DAG (1935) Berechnung verschiedener physikalischer Konstanten von heterogenen Substanzen. I. Dielektrizitätskonstanten und Leitfähigkeiten der Mischkörper aus isotropen Substanzen. *Annalen der Physik* 416: 665–679.
  39. Khomenkova L, Labbé C, Portier X, et al. (2013) Undoped and Nd<sup>3+</sup> doped Si-based single layers and superlattices for photonic applications. *Phys Stat Sol (a)* 210: 1532–1543.
  40. Campbell IH, Fauchet PM (1986) The effects of microcrystal size and shape on the one phonon Raman spectra of crystalline semiconductors. *Solid State Commun* 58: 739–741.
  41. Morales M, Leconte Y, Rizk R, et al. (2005) Structural and microstructural characterization of nanocrystalline silicon thin films obtained by radio-frequency magnetron sputtering. *J Appl Phys* 97: 034307.
  42. Schamm S, Bonafos C, Coffin H, et al. (2008) Imaging Si nanoparticles embedded in SiO<sub>2</sub> layers by (S)TEM-EELS. *Ultramicroscopy* 108: 346–357.
  43. Skuja LN, Silin AR (1979) Optical properties and energetic structure of non-bridging oxygen centers in vitreous SiO<sub>2</sub>. *Phys Stat Sol A* 56: K11–K13.
  44. Munekuni S, Yamanaka T, Shimogaichi Y, et al. (1990) Various types of nonbridging oxygen hole center in high-purity silica glass. *J Appl Phys* 68: 1212–1217.
  45. Bratus' VYa, Yukhinchuk VA, Berezhinsky LI, et al. (2001) Structural transformations and silicon nanocrystallite formation in SiO<sub>x</sub> films. *Semiconductors* 35: 821–826.
  46. Prokes SM, Carlos WE (1995) Oxygen defect center red room temperature hotoluminescence from freshly etched and oxidized porous silicon. *J Appl Phys* 78: 2671–2674.
  47. Torchyska TV, Korsunska NE, Khomekova LYu, et al. (2000) Suboxide-related centre as the source of the intense red luminescence of porous Si. *Microelectron Eng* 51–52: 485–493.
  48. Song HZ, Bao XM (1997) Visible photoluminescence from silicon-ion-implanted SiO<sub>2</sub> films and its multiple mechanisms. *Phys Rev B* 55: 6988–6993.
  49. Dubin VM, Chazalviel J-N, Ozaman F (1993) In situ photoluminescence and photomodulated infrared study of porous silicon during etching and in ambient. *J Lumin* 57: 61–65.
  50. Yin S, Xie E, Zhang C, et al. (2008) Photoluminescence character of Xe ion irradiated sapphire. *Nucl Instr Methods B* 12–13:2998–3001.
  51. Kokonou M, Nassiopoulou AG, Travlos A (2003) Structural and photoluminescence properties of thin alumina films on silicon, fabricated by electrochemistry. *Mater Sci Eng B* 101: 65–70.
  52. Dogan I, Yildiz I, Turan R (2009) PL and XPS depth profiling of Si/Al<sub>2</sub>O<sub>3</sub> co-sputtered films and evidence of the formation of silicon nanocrystals. *Physica E* 41: 976–981.
  53. Varshni YP (1967) Temperature dependence of the energy gap in semiconductors. *Physica* 34: 149–154.
  54. O'Donnell KP, Chen X (1991) Temperature dependence of semiconductor band gaps. *Appl Phys Lett* 58: 2925–2927.

55. Peng X-H, Alizadeh A, Bhate N, et al. (2007) First-principles investigation of strain effects on the energy gaps in silicon nanoclusters. *J Phys Condens Matter* 19: 266212 (9 pages).
56. Menendez J, Cardona M (1984) Temperature dependence of the first-order Raman scattering by phonons in Si, Ge, and  $\alpha$ -Sn: Anharmonic effects. *Phys Rev B* 29: 2051–2059.
57. Lautenschlager P, Garriga M, Vina L, et al. (1987) Temperature dependence of the dielectric function and interband critical points in silicon. *Phys Rev B* 36: 4821–4830.
58. Steasman A, Afanas'ev VV (1997) Point defect generation in  $\text{SiO}_2$  by interaction with SiO at elevated temperatures. *Microelectr Eng* 36: 201–204.
59. Jones BJ, Barklie RC (2005) Electron paramagnetic resonance evolution of defects at the (100)Si/ $\text{Al}_2\text{O}_3$  interface. *J Phys D Appl Phys* 38: 1178–1181.
60. Nast O, Wenham SR (2000) Elucidation of the layer exchange mechanism in the formation of polycrystalline silicon by aluminum-induced crystallization. *J Appl Phys* 88: 124–132.



AIMS Press

© 2016 Larysa Khomenkova, et al., licensee AIMS Press. This is an open access article distributed under the terms of the Creative Commons Attribution License (<http://creativecommons.org/licenses/by/4.0>)